Supplementary Information (SI)

Multiscale structural control of linked metal-organic polyhedra gel by aging-induced linkage-reorganization

Zaoming Wang,[ab] Christian Villa Santos,[c] Alexandre Legrand,[a] Frederik Haase,[a] Yosuke Hara,[d] Kazuyoshi Kanamori,[d] Takuma Aoyama,[e] Kenji Urayama,[e] Cara M. Doherty,[f] Glen J. Smales,[g] Brian R. Pauw,[g] Yamil J. Colón,[c] Shuhei Furukawa*[ab]

[a]Institute for Integrated Cell-Material Science (WPI-iCeMS), Kyoto University, Yoshida, Sakyo-ku, Kyoto 606-8501, Japan

[b]Department of Synthetic Chemistry and Biological Chemistry, Graduate School of Engineering, Kyoto University, Katsura, Nishikyo-ku, Kyoto 615-8510, Japan

[c]Department of Chemical and Biomolecular Engineering, University of Notre Dame, Notre Dame, IN 46556, USA

[d]Department of Chemistry, Graduate School of Science, Kyoto University, Kitashirakawa, Sakyo-ku, Kyoto 606-8502, Japan

[e]Department of Macromolecular Science and Engineering, Kyoto Institute of Technology, Matsugasaki, Sakyo-ku, Kyoto 606-8585, Japan

[f]Manufacturing, Commonwealth Scientific and Industrial Research Organisation, Clayton South, Victoria, Australia

[g]Bundesanstalt für Materialforschung und -prüfung (BAM), Unter den Eichen 87, 12205 Berlin, Germany

1. Materials and Characterization

Materials

Rhodium acetate was synthesized according to a previously reported procedure.[1] Isophthalic acid (H_2bdc) was purchased from Sigma-Aldrich and used as received. Solvents were purchased from Wako Pure Chemical Industries except those at HPLC grade which were purchased from Fischer Chemicals.

Characterizations

The rheological measurements of the gels were made using a stress-controlled AR-G2 (TA Instruments, New Castle, DE, USA) rheometer. Gel samples after synthesis or aging were pushed out from the syringe (the syringe head was cut) and carefully transferred into a clean glass slide (~ 1 mm in thickness). Then the gel was loaded into the rheometer with the glass slide to perform the rheology tests. The measurements of gels were conducted by frequency sweeping in a compression mode with a 1% strain amplitude that was well inside the linear regime (initial strain is fixed to 1.5%).

The super-critical CO_2 drying process was carried out on SCLEAD-2BD autoclave (KISCO) using super-critical CO_2 at 14 MPa and 50 °C.

Infrared (IR) spectroscopy data were recorded in ATR mode using a Jasco FT/IR-6100 with 1 cm^{-1} resolution and an accumulation of 128 scans. UV-vis was measured in a V-670 spectrophotometer (JASCO).

Scanning Electron Microscopy (SEM) of the microstructures of the aerogel samples were observed using a field-emission scanning electron microscope with a JEOL Model JSM-7001F4 system operating at 10 kV and 5 mA current. The samples were coated with 28 nm Osmium before measurement.

^{1}H NMR spectra were recorded on a Bruker Biospin DRX-600 (600 MHz) spectrometer. For ^{1}H-NMR analysis, 5 mg of aerogel sample was digested in a mixture of DMSO-d_6 (750 µl) and DCl (50 µl). The mixture was then heated at 100 °C overnight to obtain a yellow solution.

N_2 (77 K) gas sorption isotherms of the MOPs and aerogels were recorded on a BELSORP-max

volumetric adsorption instrument from BEL Japan Inc. Prior to gas sorption measurement, the samples were activated at 120 °C for 12 h.

Thermogravimetric analyses (TGA) of the MOPs and aerogels were performed in the temperature range from room temperature to 500 ºC at a heating rate of 10 ºC/min with a Rigaku Thermo plus EVO2, under a nitrogen atmosphere.

Time-resolved dynamic light scattering (TRDLS) experiment were performed on a Zetasizer Nano ZS instrument (Malvern Instruments, Malvern, UK). The light source was a HeNe laser working at $\lambda = 633$ nm. The observations were made at the backscattering angle $\theta = 173^{o}$. The time dependence of particle size and the time-averaged scattering intensity during gelation process was evaluated at 80 ºC for 25 min.

The skeletal density of the aerogels was measured by helium pycnometry from Ultrapyc 1200e, Quantachrome Instruments, USA. For the neat HRhMOP, the skeletal density was estimated by the crystal data obtained from SCXRD.

The bulk density of the aerogels was determined by dividing the volume of **Gel-*n*** by the weight of the corresponding aerogel. The volume of **Gel-*n*** after synthesis and aging was calculated from the height and diameter of the wet gel by Vernier caliper (as seen in Figure S4). After super-critical CO_2 drying, the corresponding aerogels were weighted for density calculation. For the neat **HRhMOP**, the bulk density was estimated by the crystal data obtained from SCXRD.

Positron annihilation lifetime spectroscopy (PALS) experiments were conducted on EG&G Ortec Spectrometer. A 1.5 MBq ^{22}NaCl positron source sealed between two sheets of 2.54 μm Mylar was positioned in the center of two Al sample holders. Lifetimes were collected at 298K where a minimum of 5 files of 1 x 10^6 integrated counts was collected over 24h and analyzed using LT v9 software.[2] The data was fitted to 3 lifetimes: the first lifetime, $\tau 1$ was attributed to *para*-positronium (*p*-Ps) annihilation and fixed to 0.125 ns. The second lifetime, $\tau 2$ due to the free annihilation of the positron with free electrons within the sample, was approximated to 0.4 ns. The final lifetime, $\tau 3$, was associated with *ortho*-positronium (*o*-Ps) annihilation and fitted as a discrete lifetime and attributed to the pores within the aerogels. An extra *o*-Ps component was observed for the neat **HRhMOP** sample.

The small-/wide-angle X-ray scattering (SAXS/WAXS) measurements were conducted using the MOUSE (Methodology Optimization for Ultrafine Structure Exploration). X-rays were generated from a microfocus X-ray tube, followed by multilayer optics to parallelize and monochromatize the X-ray beams to a wavelength of Cu Kα (λ = 0.154). Scattered radiation was detected on an in-vacuum Eiger 1M detector (Dectris, Switzerland), which was placed at multiple distances between 137 - 2507 mm from the sample. All samples were mounted in the sample chamber between two strips of Scotch Magic tape.[3] The resulting data has been processed and scaled to absolute intensity using the DAWN software package in a standardized complete 2D correction pipeline with uncertainty propagation.[4-5] The data was fitted and analyzed using McSAS, a Monte Carlo method to extract form-free size distributions.[6]

2. Synthesis

Synthesis of precursors

1-dodecyl-1H-imidazole (**diz**), 1,4-bis(imidazole-1-ylmethyl)benzene (**bix**) and **HRhMOP** were synthesized according to our previous reports.[7-8]

Synthesis of HRhMOP(diz)$_{12}$

200 mg of **HRhMOP** were dispersed in 40 mL of DCM, then 132.5 mg of **diz** (18 mol. eq.) were added. After sonication for 5 mins, the solution was centrifuged to remove the precipitate. The upper purple solution was collected and evaporated in vacuum. The obtained solid residue was washed twice with EtOH to remove any remaining **diz**. Finally, the purple solid product was dried under vacuum.

Synthesis of Gel-*n*

In a typical synthesis process, 1 mL DMF solution of **HRhMOP(diz)$_{12}$** (2.8 mM) was added to 1 mL DMF solution of **bix** (33.6 mM, 12 mol. eq.) under vigorous stirring. The resultant transparent purple solution was transferred into the sealed syringe and placed in a preheated oven at 80 °C where it gelated within minutes. The sample was further heated at 80 °C for 8 h for a complete reaction. After the gelation, 5 mL of fresh DMF was added into the gel-holding syringe, which was then heated at 80 °C for 8 h to achieve 1 aging cycles, followed by the removal of the excessive DMF added. The same procedure was repeated in order to obtain gel samples at different aging cycles, and the corresponding gels were named as **Gel-*n*** where n indicates the number of aging cycles applied.

Synthesis of Aerogel-*n*

To obtain aerogel samples for further analysis, aged **Gel-*n*** was soaked with acetone for three days with replacing the fresh acetone each day. Then the solvent-exchanged sample was dried by supercritical CO_2 at 14 MPa and 50 °C for 90 min to obtain **Aerogel-*n***. Prior to sorption measurements, the aerogel sample was activated at 120 °C under vacuum for 12 h.

3. Estimation of network branch functionality (*f*) from the gel composition obtained by NMR

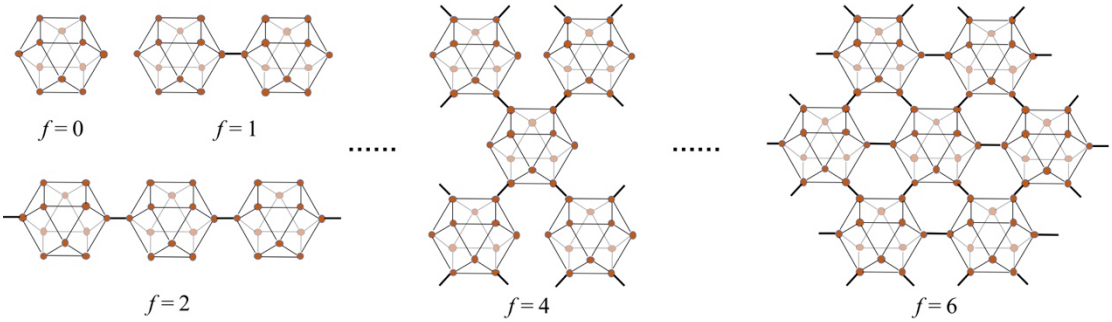

Figure S1. Illustrated MOPs interlinking with different network branch functionality, *f*.

Network branch functionality, *f* is the average number of bridges that connect network junctions.[9] In this paper, it is applied to indicate the number of Rh sites per MOP which were used to bridge other MOPs. Based on the gel composition obtained from the ^{1}H NMR analysis of the acid-digested aerogels, the corresponding *f* could be calculated by the following equation:

$$f = 2 \times (12 - n_{bix} - n_{diz})$$

where n_{bix} and n_{diz} is the average number of **bix** and **diz** coordinated on MOPs obtained from the ^{1}H NMR experiment. The calculated results are listed in Table 1 and shows that aging process leads to an increase of *f* and thus further crosslinking of MOPs in the linked MOP gels. As shown in Figure S1, the structure of the network would be strongly affected by *f*, and the theoretical maximum value of *f* in this system is 12, where all outer Rh sites are used to link with surrounded MOPs.

4. Supplemental Figures

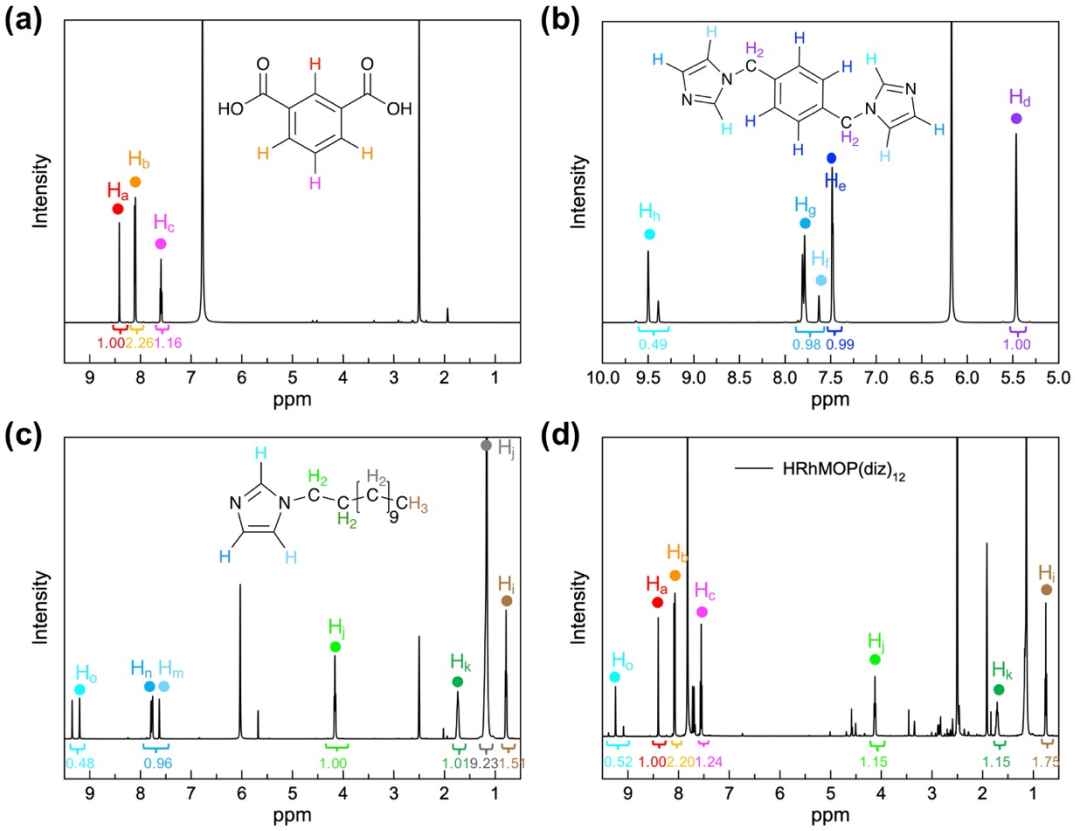

Figure S2. (a) ^{1}H NMR spectrum of **bdc** treated with the same conditions used to digest **Aerogel-*n***. (b) ^{1}H-NMR spectrum of **bix** treated with the same conditions used to digest **Aerogel-*n***. (c) ^{1}H-NMR spectrum of **diz** treated with the same conditions used to digest **Aerogel-*n***. (d) ^{1}H NMR spectrum of the acid digested **HRhMOP(diz)$_{12}$**. The distinctive protons H_a, H_b and H_c for **HRhMOP**, H_i, H_j, H_k and H_o for **diz** were used to calculate the molecular formula of the resulting **HRhMOP(diz)$_{12}$** for integration. As labeled in the figure, several protons were used for each compound and their integrations were averaged for accuracy. Following this methodology, the number of **diz** molecules per **HRhMOP** in **HRhMOP(diz)$_{12}$** was estimated to be ~11.9, which is very closes to the theoretical 12.

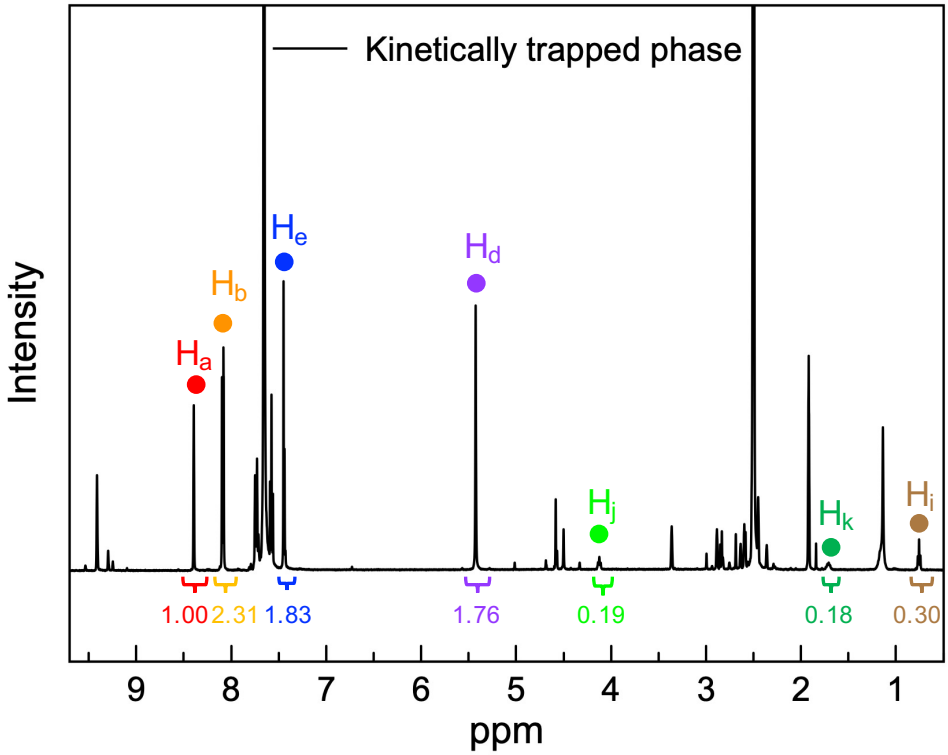

Figure S3. ^{1}H NMR spectrum of the acid digestion of kinetically trapped phase obtained immediately after adding 12 mol eq. of bix to **HRhMOP(diz)$_{12}$**. The peaks chosen for integration of each component (**HRhMOP**, **bix** and **diz**) are marked by different colors and corresponded to the protons of pure compounds in Figure S2. The distinctive protons H_a and H_b for **HRhMOP**, H_d and H_e for **bix**, H_i, H_j and H_k for **diz** were used to calculate the molecular formula of the resulting sample for integration. Several protons were used for each compound and their integrations were averaged for accuracy. Following this methodology, the composition of the kinetically trapped molecules was estimated as **HRhMOP(bix)$_{10.0}$(diz)$_{2.1}$** with the number of ligands per MOP to be ~12.1, which is very closes to the theoretical 12.

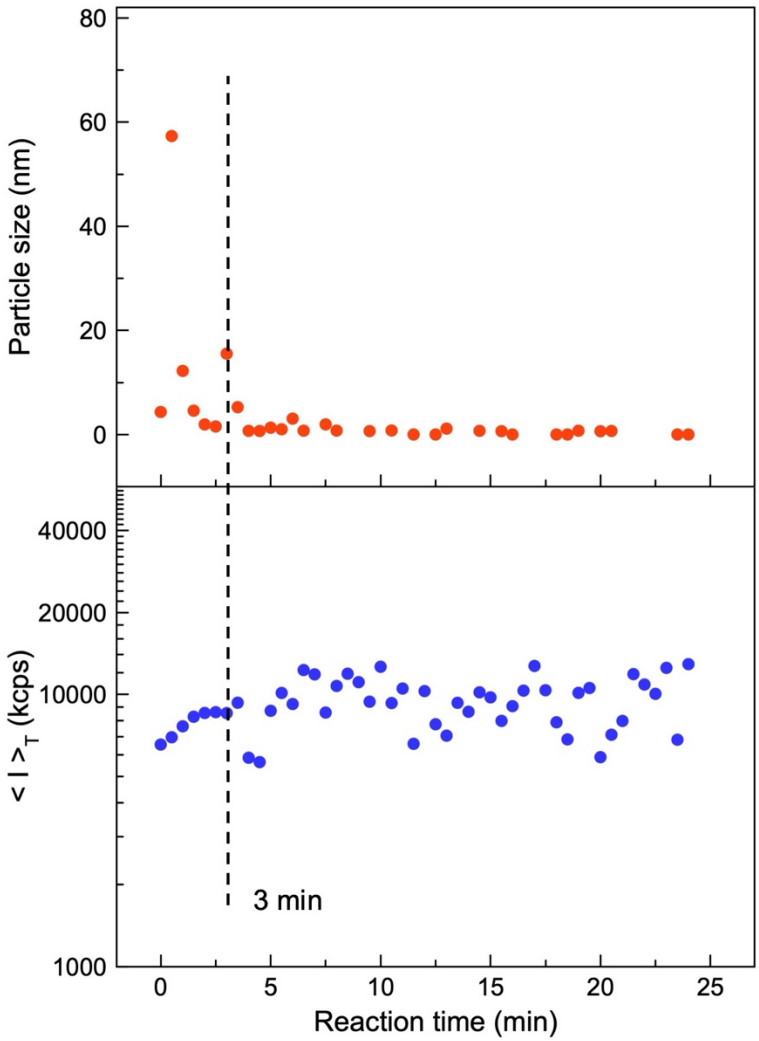

Figure S4. Time-resolved dynamic light scattering (TRDLS) experiments during the supramolecular polymerization of MOPs at 80 ºC at a concentration of 1.4 mM, showing the particle size evolution (upper) and the time-averaged scattering intensity (bottom) as a function of time. Once the polymerization begins, the trapped MOP molecules are hierarchically assembled into colloidal particles, leading to a steep increase in particle size. By further forming colloidal networks, the general mobility of the particles is frozen and the diffusion is stopped, rendering reliable measurement of the particle size impossible. As shown in the top figure, the gelation occurring here is too fast to observe the gradual increase in size, making it difficult to estimate the sol-gel transition point. To determine this gelation point, change in the time-averaged scattering intensity, $\langle I \rangle_T$, were plotted as a function of time, where the time at which random fluctuations appear corresponds to the gelation point. The result shows that the kinetically trapped phase used here gelated in 3 mins.

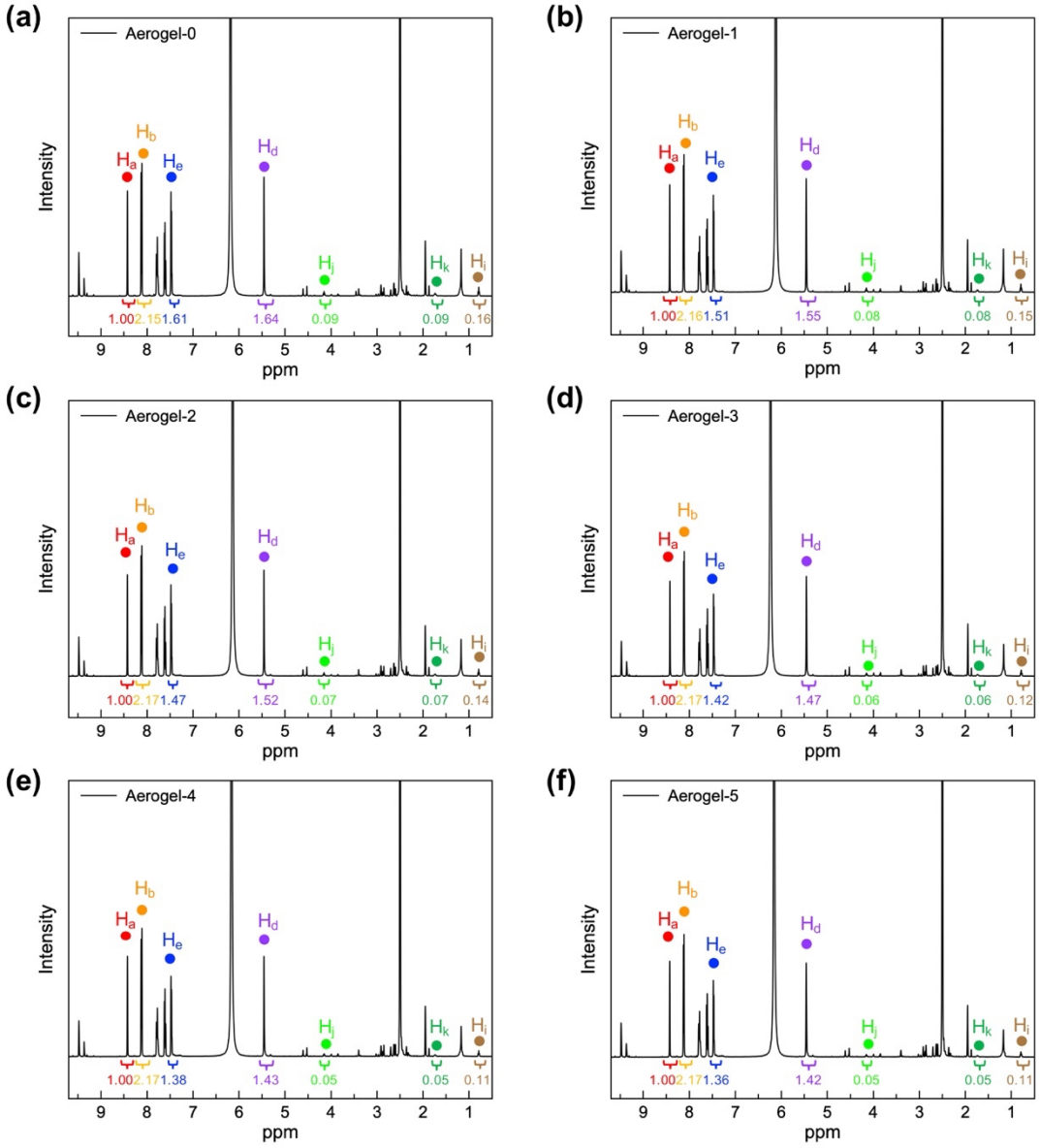

Figure S5. ^{1}H NMR spectrum of the acid digested **Aerogel-*n***. The peaks chosen for integration of each component (**HRhMOP**, **bix** and **diz**) are marked by different colors and corresponded to the proton of compound in Figure S3. The distinctive protons H_a and H_b for **HRhMOP**, H_d and H_e for **bix**, H_i, H_j and H_k for **diz** were used to calculate the molecular formula of the resulting aerogels for integration. Several protons were used for each compound and their integrations were averaged for accuracy. Following this methodology, the compositions of each aerogel samples were estimated as shown in Table 1.

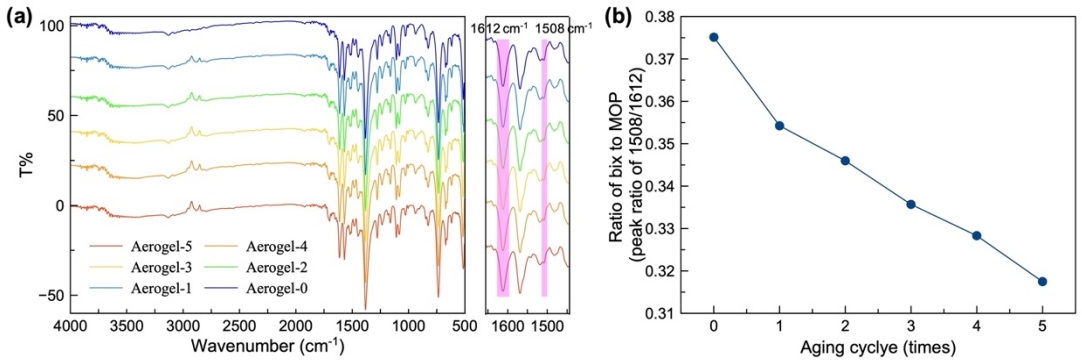

Figure S6. (a) IR spectra of **Aerogel-*n***; (b) Evolution of the intensity ratio of peaks at 1508 cm^{-1} and 1612 cm^{-1} in **Aerogel-*n*** as a function of the aging cycles. The peaks at 1508 cm^{-1} and 1612 cm^{-1} correspond to the characteristic vibrational bonds of C=N in **bix** and C=O in **HRhMOP**, respectively. The decreased value of the ratio as increasing aging cycles indicates that the number of **bix** molecules inside the gel networks is effectively reduced by repeated aging cycles.

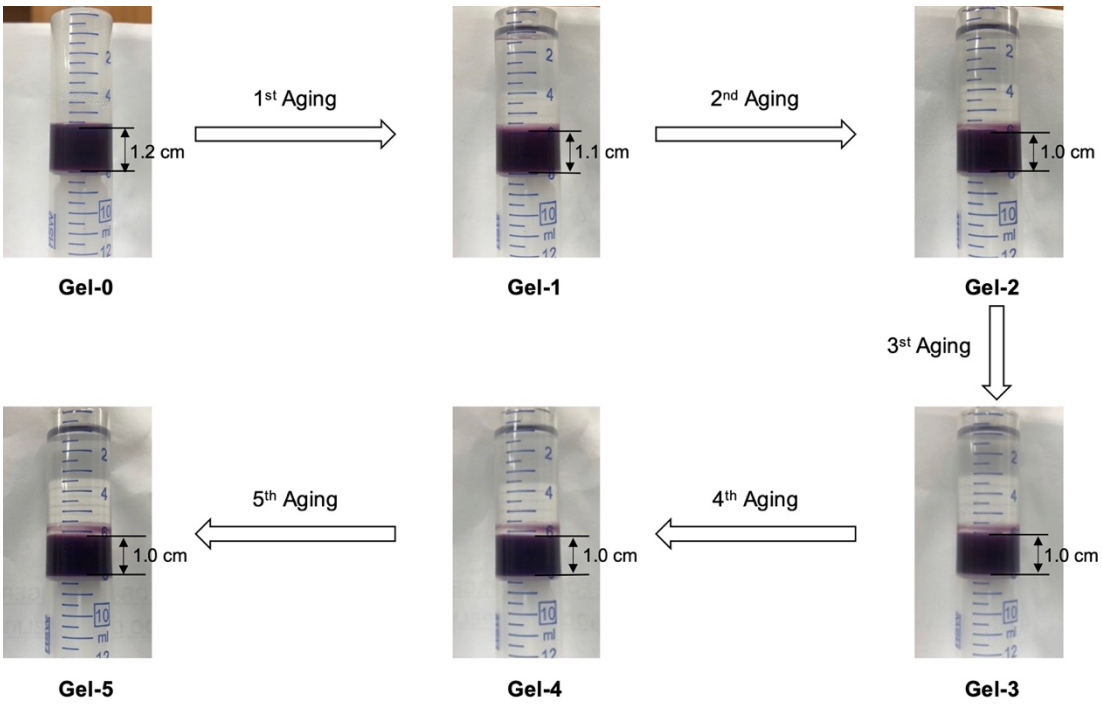

Figure S7. Pictures of a gel sample treated with repeated aging process, during which a shrinkage of the gel in volume was observed. For each aging cycle, ~5 mL fresh DMF was added prior to the heating treatment and then removed after 8 h of heating at 80 ºC.

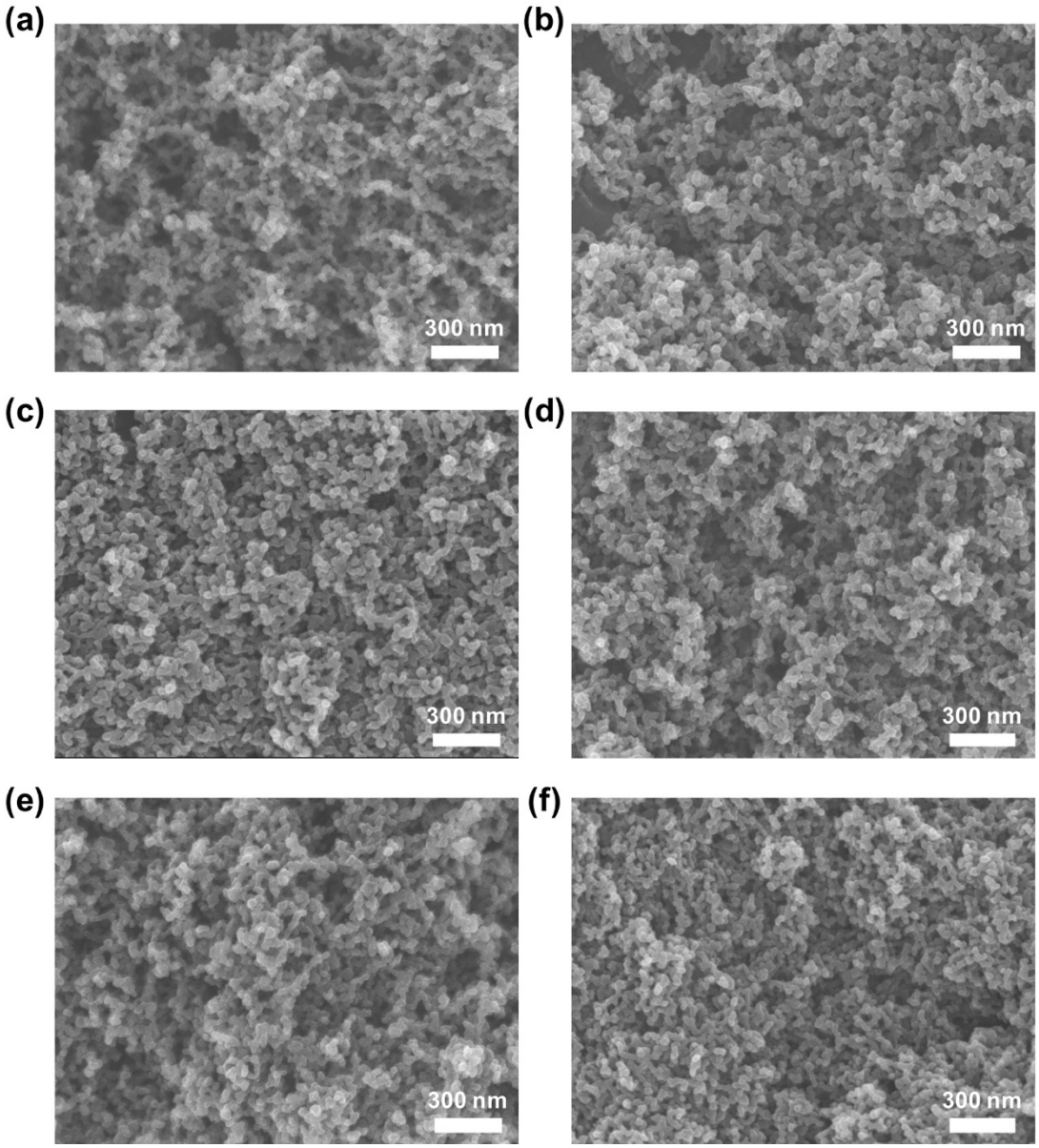

Figure S8. SEM images of (a) **Aerogel-0**, (b) **Aerogel-1**, (c) **Aerogel-2**, (d) **Aerogel-3**, (e) **Aerogel-4** and (f) **Aerogel-5**.

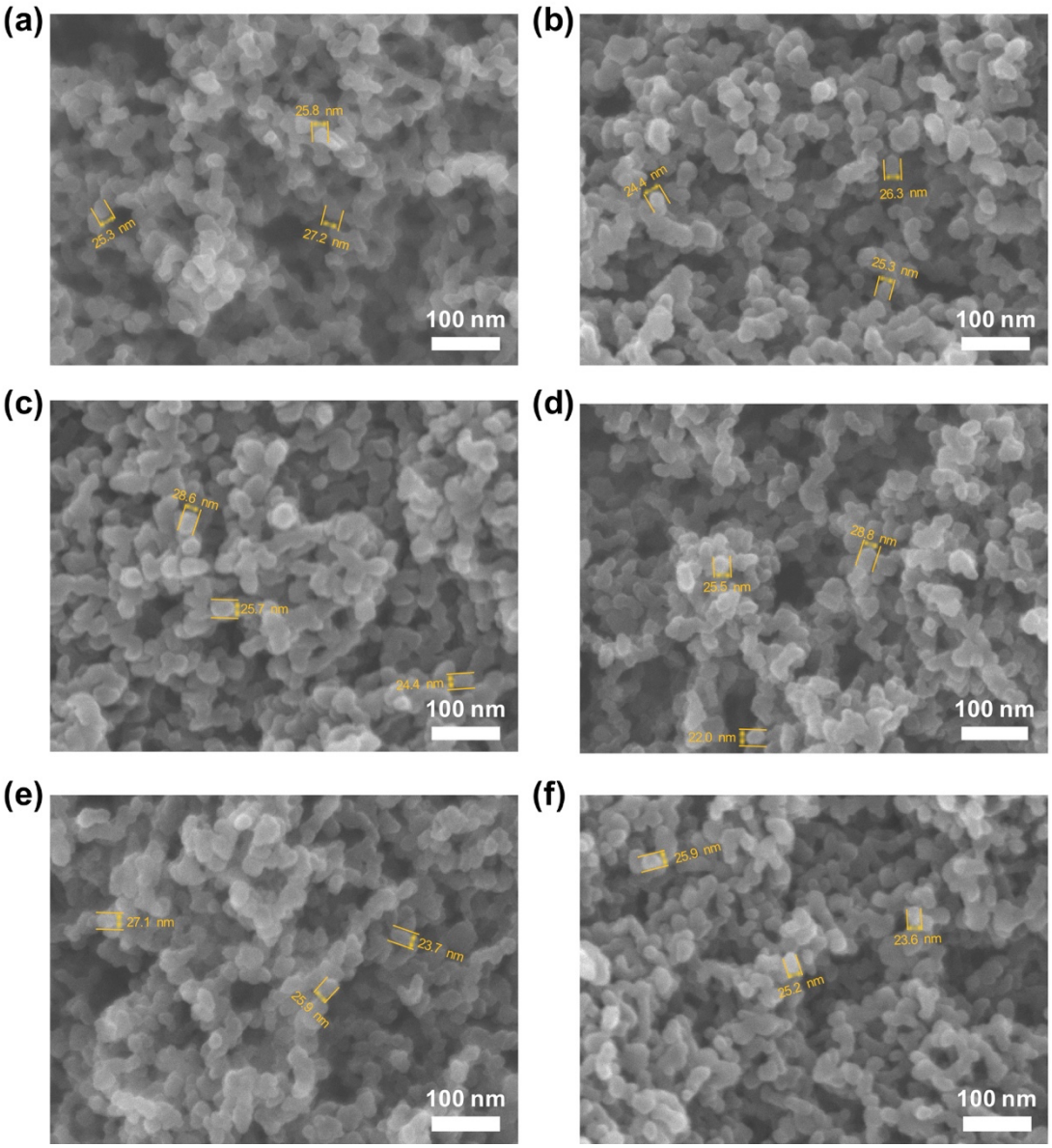

Figure S9. SEM images of (a) **Aerogel-0**, (b) **Aerogel-1**, (c) **Aerogel-2**, (d) **Aerogel-3**, (e) **Aerogel-4** and (f) **Aerogel-5** at the larger magnification.

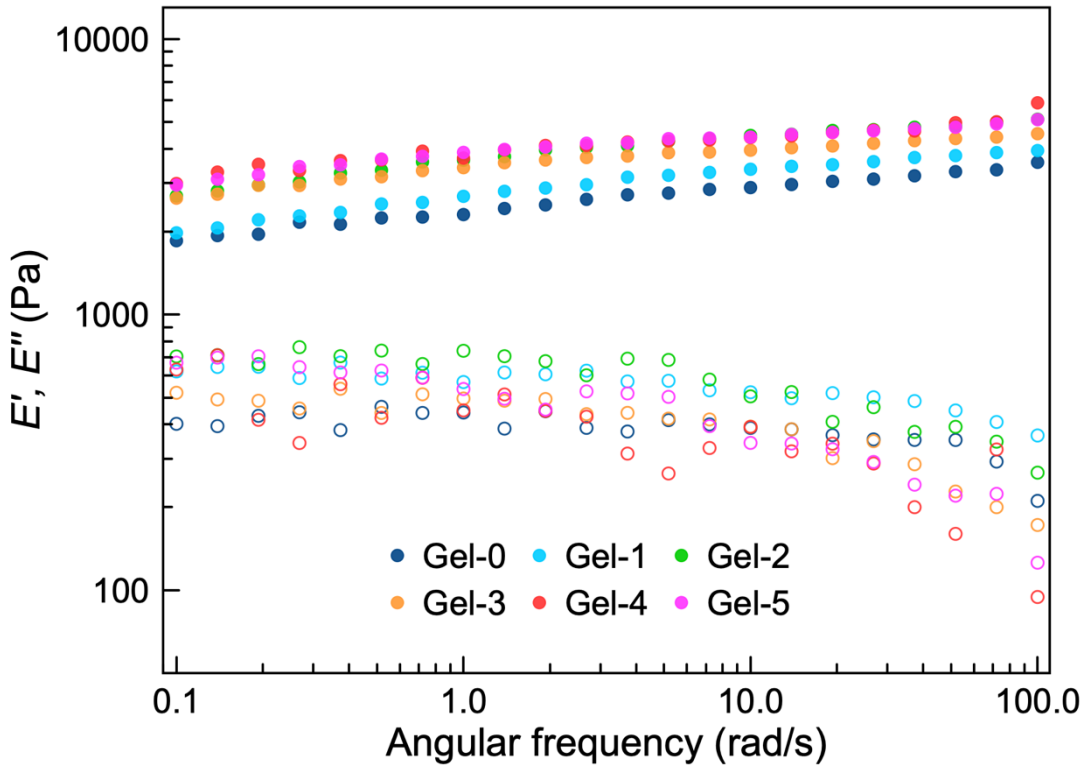

Figure S10. Storage Young's modulus (E') (filled circles) and loss Young's modulus (E'') (hollow circles) of **Gel-*n*** versus scanning frequency (ω).

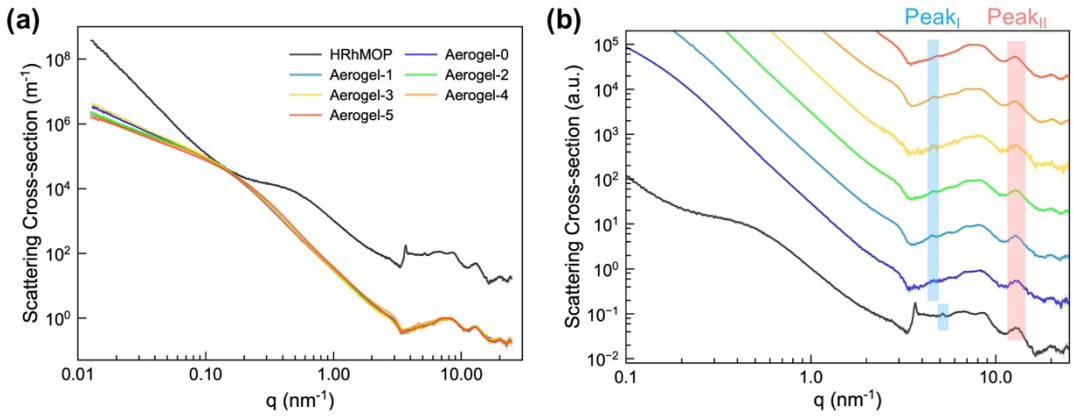

Figure S11. (a) Raw data of the SXAX/WAXS curves of **HRhMO**P and **Aerogel-*n***. (b) Zoom in of the WAXS curves of **HRhMO**P and **Aerogel-*n*** (the data was stacked for clarity)

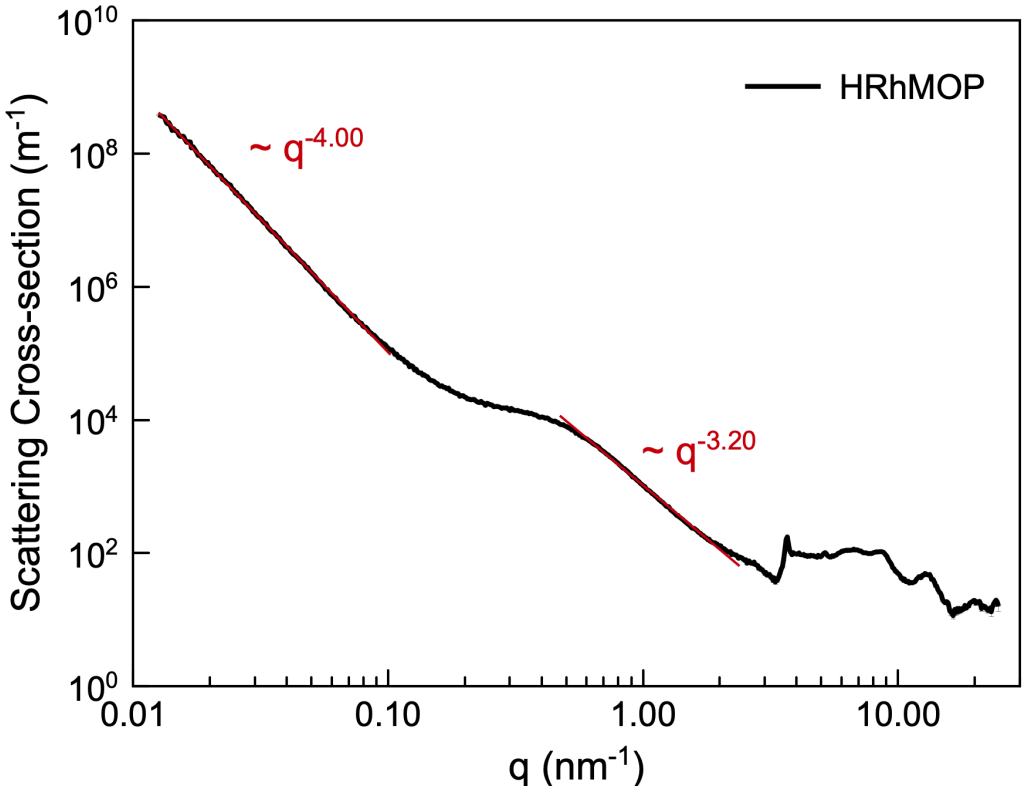

Figure S12. Fitting of the SAXS pattern for neat **HRhMOP** by power-law approximation

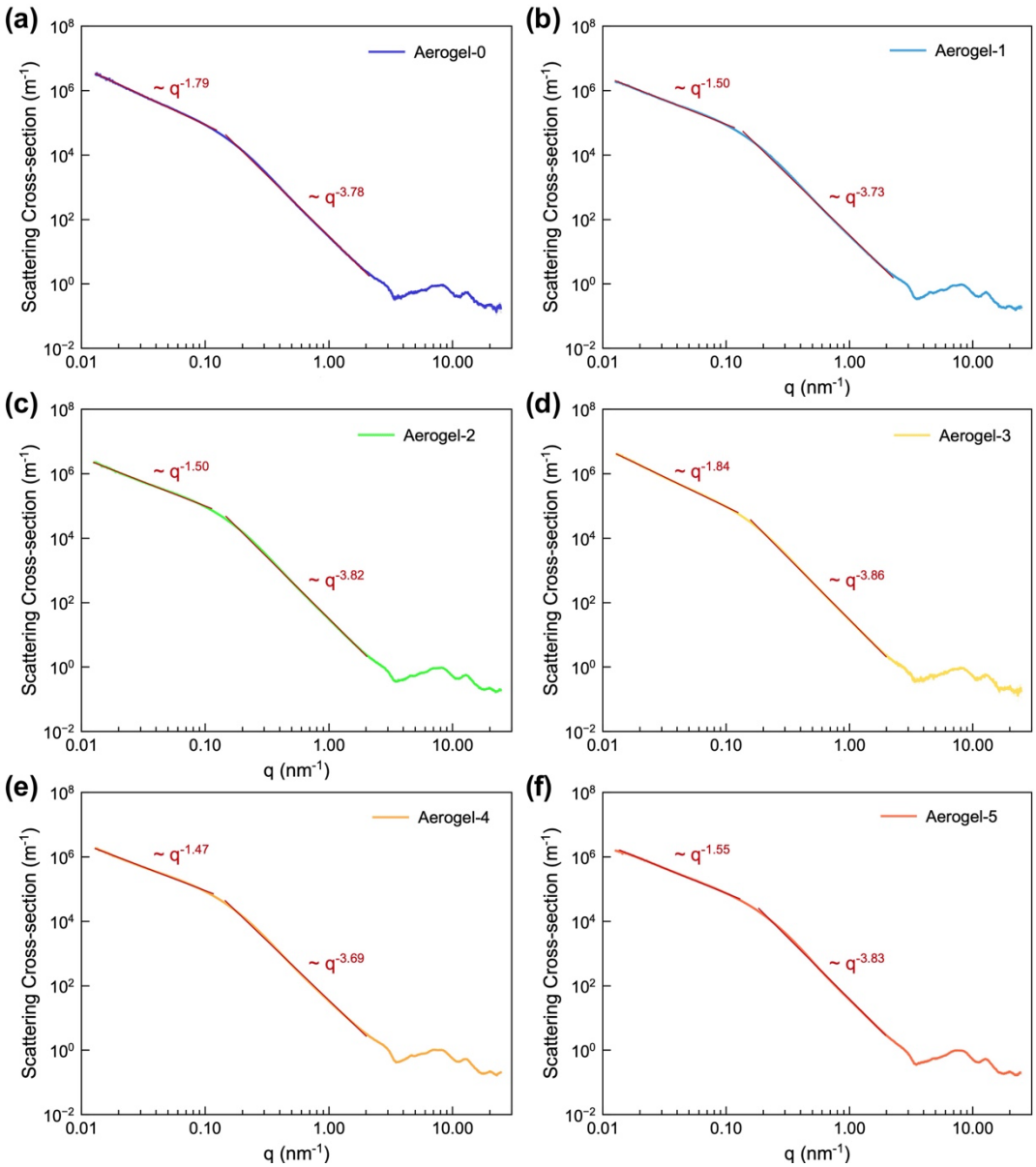

Figure S13. Fittings of the SAXS patterns for **Aerogel-*n*** by power-law approximation

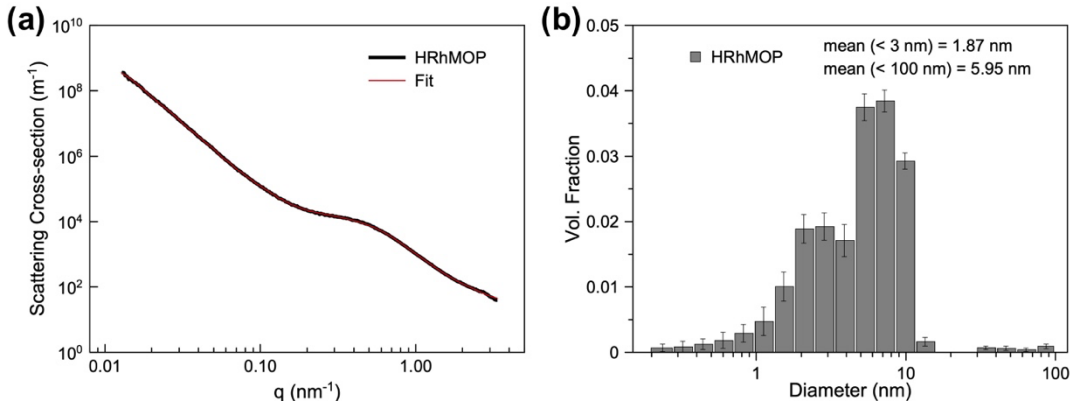

Figure S14. (a) Fitting of the SAXS pattern for neat **HRhMOP** using Monte Carlo methods and (b) the corresponding volume-weighted size distribution extracted.

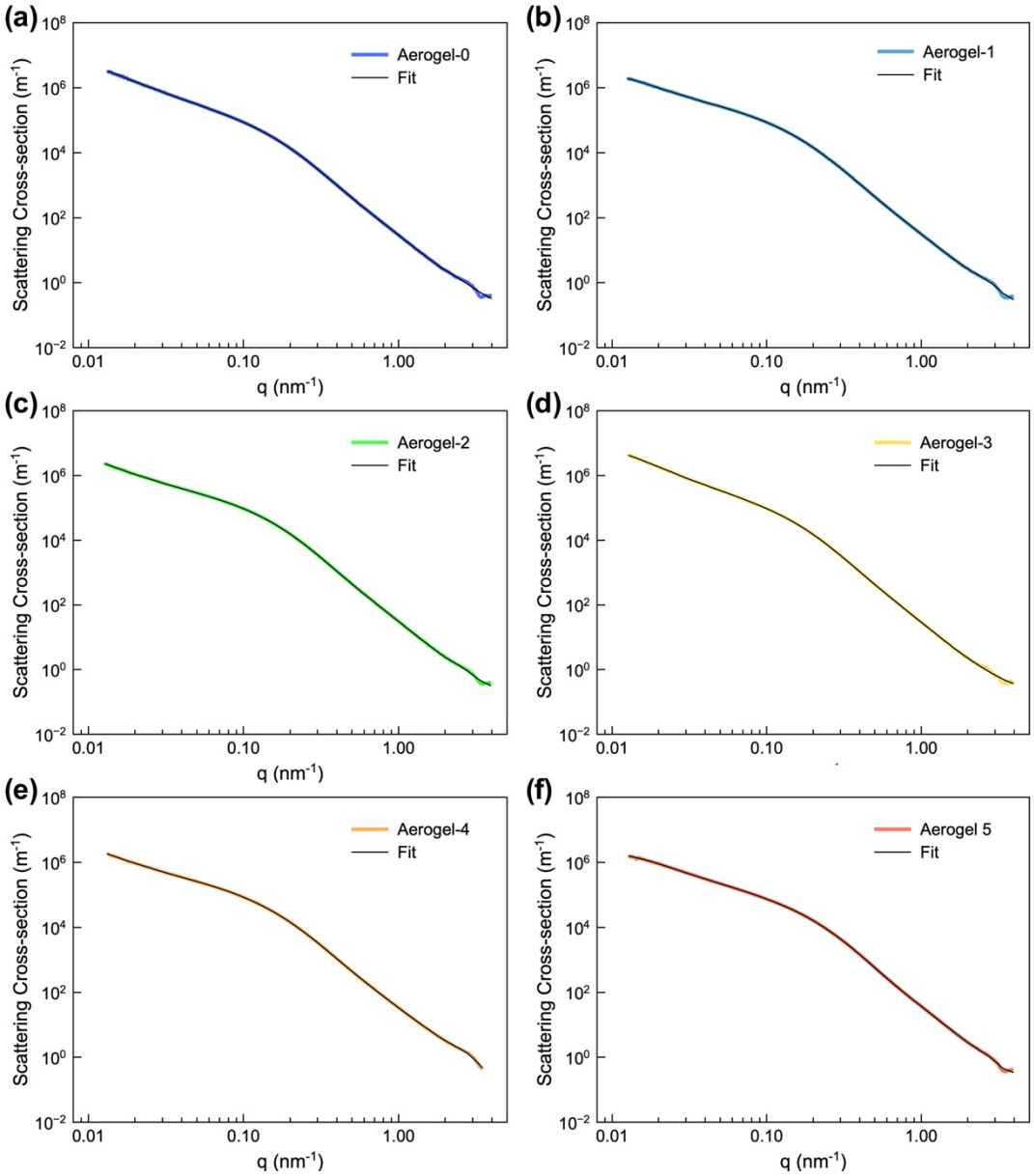

Figure S15. Fittings of the SAXS patterns for **Aerogel-*n*** using Monte Carlo methods.

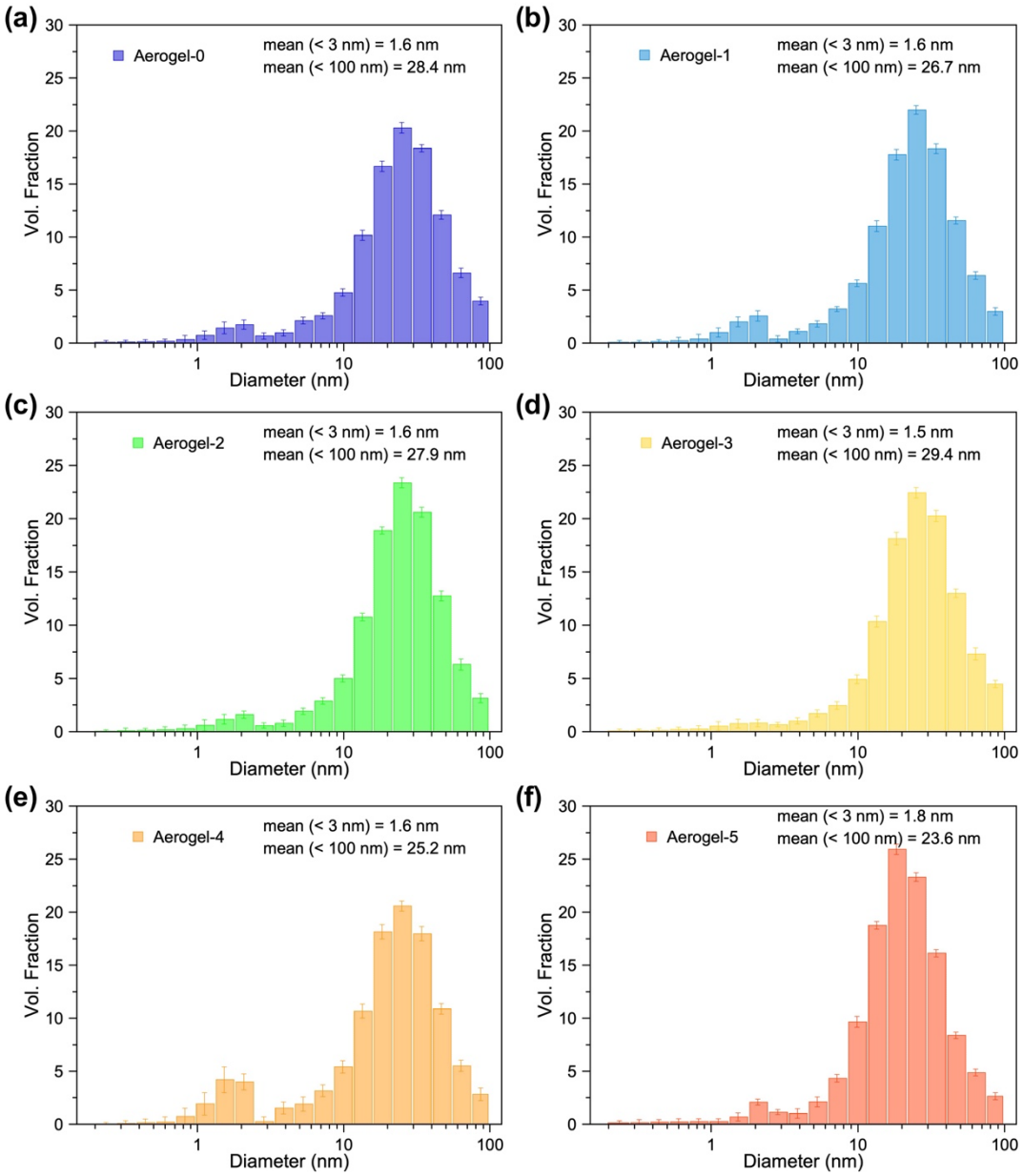

Figure S16. Volume-weighted size distributions of **Aerogel-*n*** extracted from SAXS fit using Monte Carlo methods.

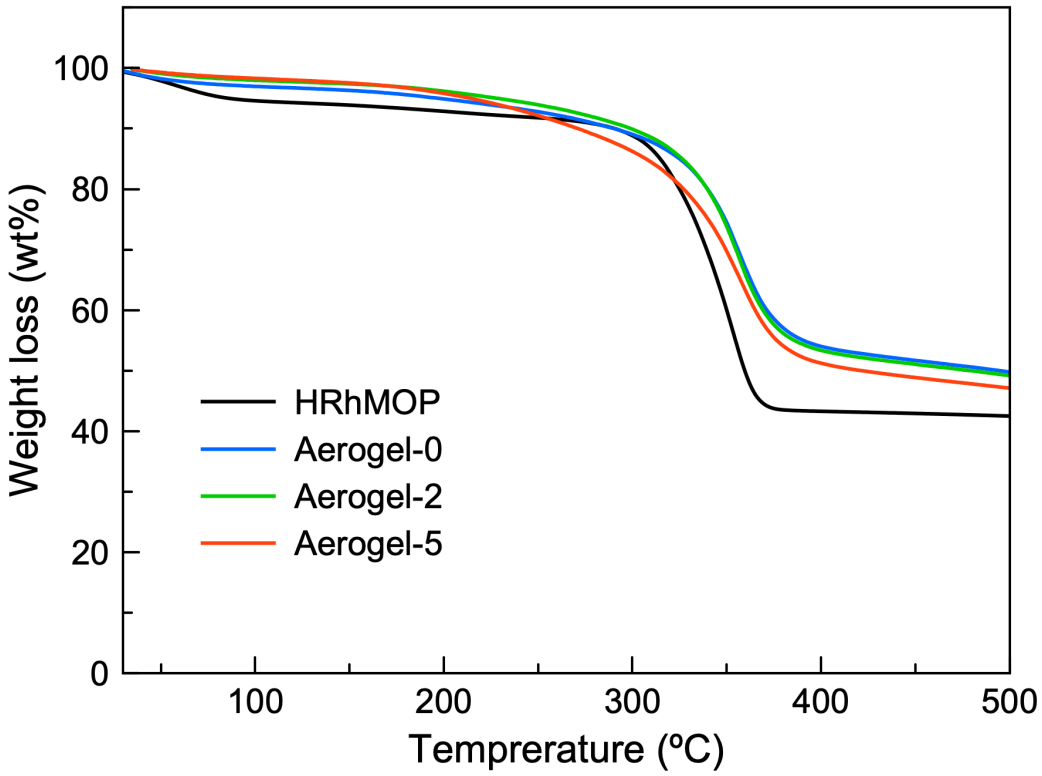

Figure S17. Thermogravimetric analysis (TGA) of **Aerogel-0**, **Aerogel-2**, **Aerogel-5** and **HRhMOP**.

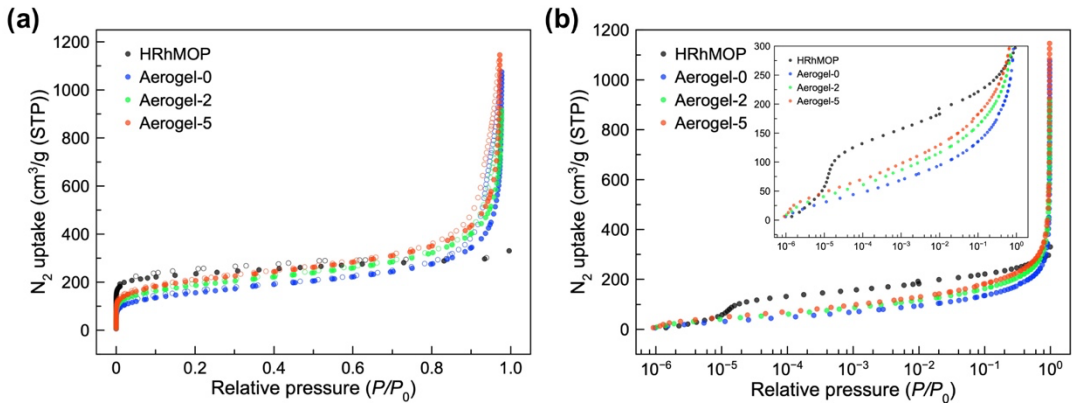

Figure S18. N_2 uptake of **Aerogel-0**, **Aerogel-2**, **Aerogel-5** and **HRhMOP** at 77 K in (a) linear and (b) semi-logarithmic plots.

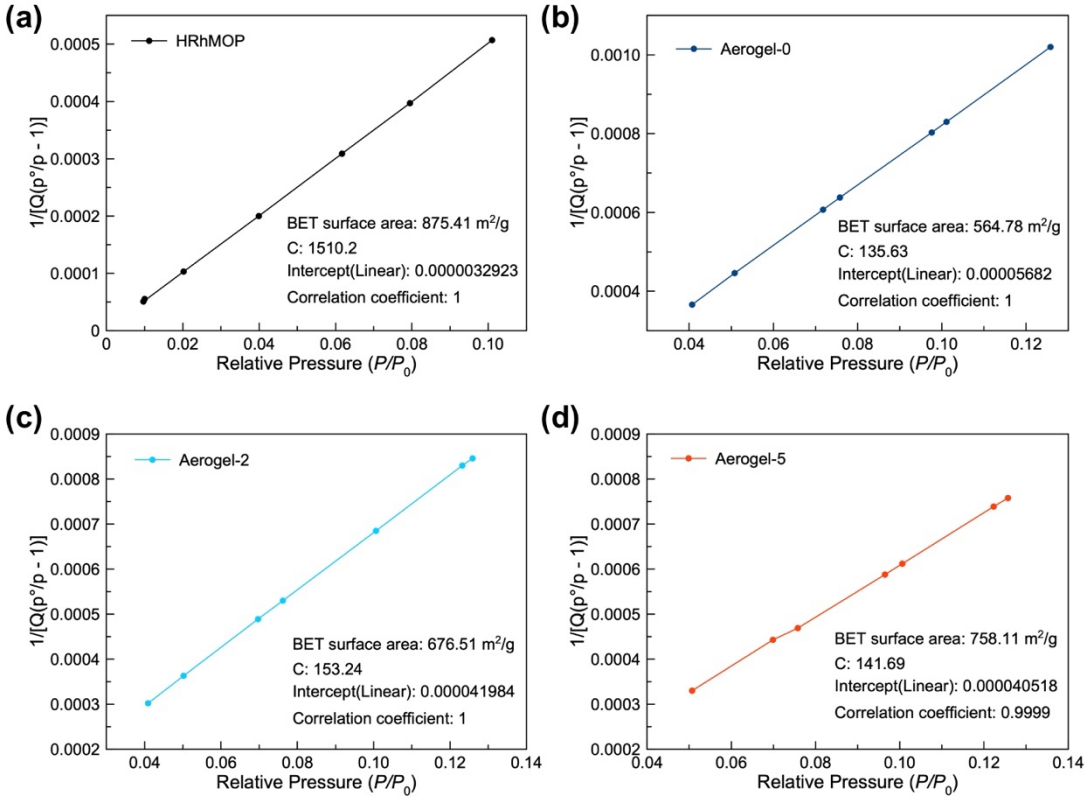

Figure S19. Calculation of the BET surface area of (a) **HRhMOP**, (b) **Aerogel-0**, (c) **Aerogel-2** and (d) **Aerogel-5**.

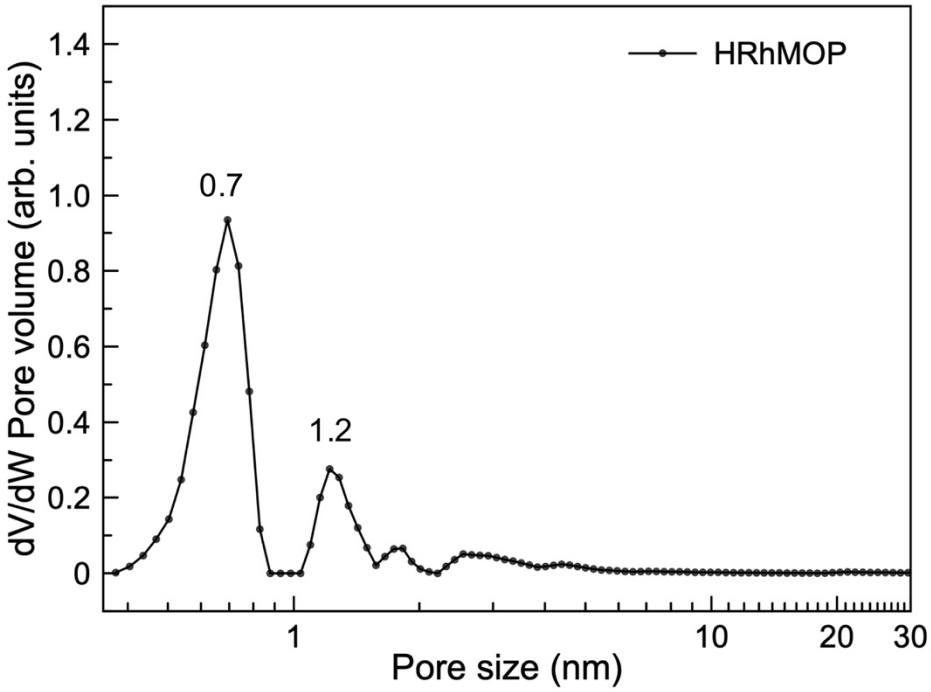

Figure S20. Pore size distribution (PSD) of the pristine **HRhMOP** estimated from the isotherm data illustrated in Figure 4a and Figure S10 by NLDFT on a slit pore model.

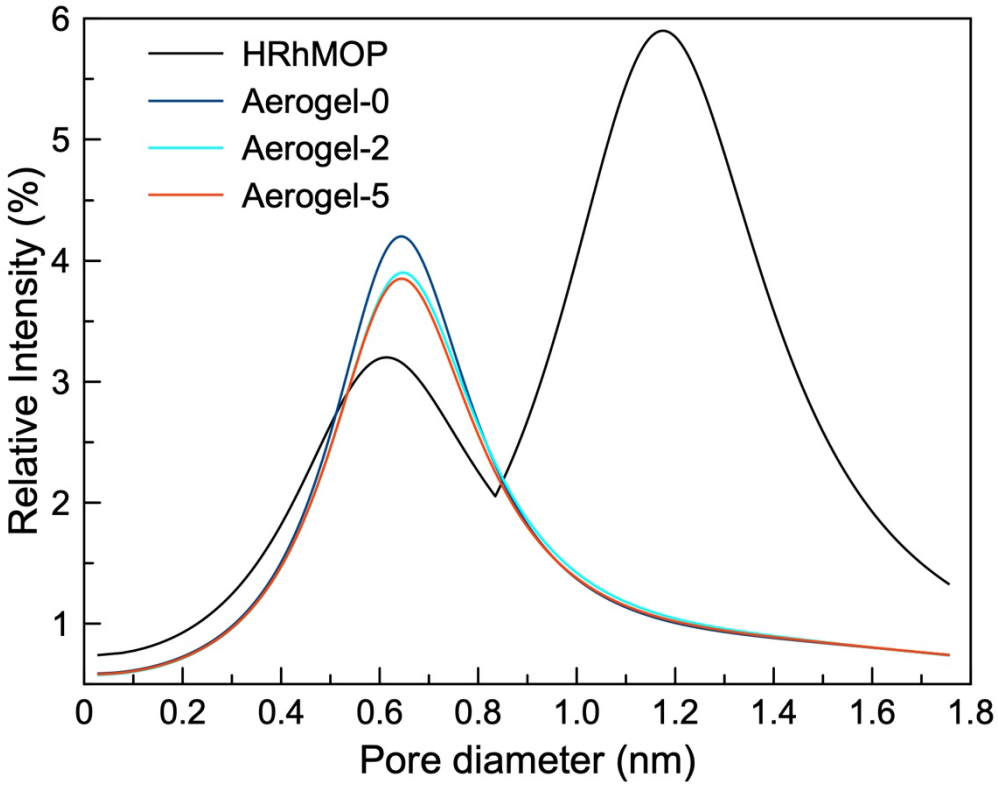

Figure S21. Pore size distribution (PSD) derived from the data of positron annihilation lifetime spectroscopy (PALS) of **HRhMOP** and **Aerogel-*n***.

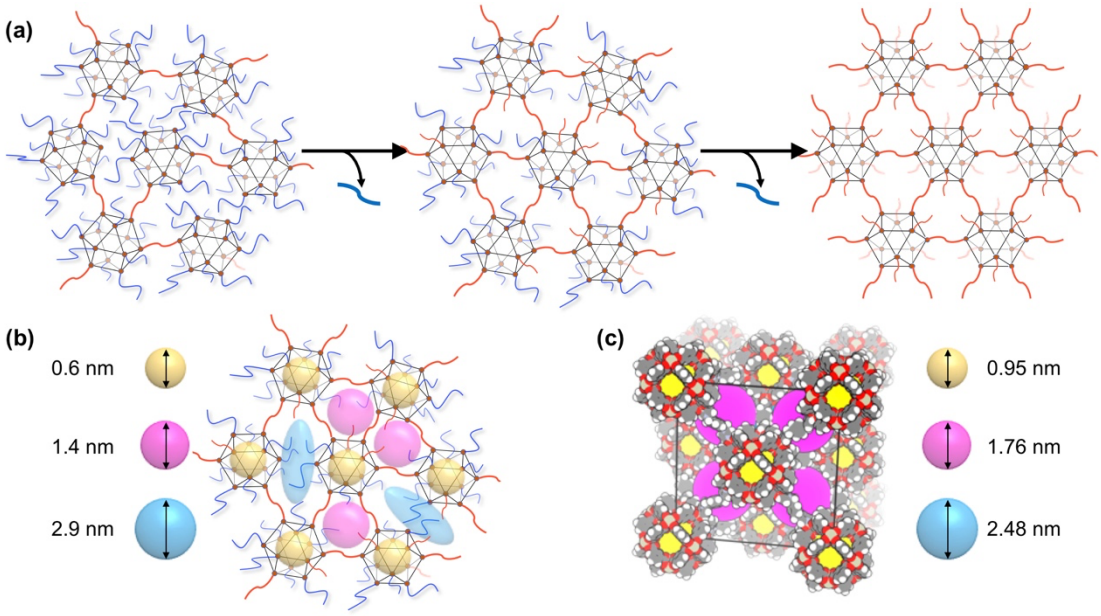

Figure S22. (a) Schematic illustration of the molecular scale rearrangement of linked MOPs induced by aging process. Schematic representation of the porous structure of (b) the linked MOP aerogels after aging and (c) the simulated crystalline network of **HRhMOP(bix)$_6$** in which each MOP is fully linked by **bix**. The different pores in these networks are marked by different colors.

Table S1. Average number of **diz** and **bix** per MOP and the resulting *f* of the aerogel at different aging cycles (each result was obtained by three replicates of ^{1}H NMR experiment of the corresponding aerogel samples).

Sample	Number of **diz** per MOP	Number of **bix** per MOP	*f*
Aerogel-0	1.3 ± 0.1	9.6 ± 0.5	2.2 ± 1.0
Aerogel-1	1.3 ± 0.2	9.2 ± 0.4	3.1 ± 1.0
Aerogel-2	1.3 ± 0.2	8.7 ± 0.4	4.0 ± 0.9
Aerogel-3	1.2 ± 0.3	8.4 ± 0.2	4.7 ± 0.7
Aerogel-4	1.1 ± 0.3	8.2 ± 0.2	5.5 ± 0.6
Aerogel-5	0.8 ± 0.1	7.9 ± 0.3	6.6 ± 0.7

Table S2. Form-free size distribution, power coefficient (slope) and mass fractal dimension of **HRhMOP** and **Aerogel-*n*** obtained from the SAXS fits by Monte Carlo methods and power law approximation, respectively.

Sample	Mean diameter (< 3 nm)	Mean diameter (< 100 nm)	Slope (low-*q*)	Mass fractal dimension (D_m)	Slope (high-*q*)
HRhMOP	1.87 ± 0.35 nm	5.95 ± 0.11 nm	-4.0	-	-3.20
Aerogel-0	1.63 ± 0.07 nm	28.40 ± 0.12 nm	-1.79	1.79	-3.78
Aerogel-1	1.62 ± 0.05 nm	26.72 ± 0.13 nm	-1.50	1.50	-3.73
Aerogel-2	1.64 ± 0.07 nm	27.86 ± 0.12 nm	-1.50	1.50	-3.82
Aerogel-3	1.54 ± 0.09 nm	29.36 ± 0.10 nm	-1.84	1.84	-3.86
Aerogel-4	1.57 ± 0.04 nm	25.24 ± 0.16 nm	-1.47	1.47	-3.69
Aerogel-5	1.80 ± 0.09 nm	23.64 ± 0.09 nm	-1.55	1.55	-3.83

Table S3. Density and pore parameters of **HRhMOP**, **Aerogel-0**, **Aerogel-2** and **Aerogel-5**.

Sample	Volume (cm^3)	Weight (mg)	Bulk density[a] (g/cm^3)	Skeletal density[b] (g/cm^3)	Porosity[c] (%)	BET surface area[d] (m^2/g)	Total pore volume[e] (cm^3/g)
HRhMOP	-	-	1.031	1.17	12.20	875	0.51
Aerogel-0	2.12	22.5	0.0106	2.38±0.20	99.58	565	1.66
Aerogel-2	2.22	23.5	0.0106	2.19±0.13	99.55	677	1.42
Aerogel-5	2.23	25.4	0.0114	2.21±0.11	99.64	758	1.77

Note:

[a]Bulk density was determined by measuring the volume of the **Gel-*n*** and the weight of corresponding **Aerogel-*n***. For **HRhMOP**, it was calculated by the crystal data obtained from SCXRD;

[b] Skeletal density was obtained by helium pycnometry by assuming that there is only negligible difference between DMF gel and dried aerogel. For **HRhMOP**, it was calculated by the crystal data obtained from SCXRD;

[c] Porosity was calculated by $P = 100 \times (1 - \text{bulk density}/\text{skeletal density})$;

[d] BET surface area was obtained from N_2 isotherm measurement;

[e] Total pore volume was determined from N_2 isotherm measurement.

Table S4. Summary of PALS results

Sample	Lifetime of τ 3 (ns)	Intensity (%)	Average pore size in diameter (nm)
HRhMOP	2.309 ± 0.321;	3.2 ± 0.4;	0.624 ± 0.053;
	8.192 ± 0.721	5.9 ± 0.4	1.198 ± 0.048
Aerogel-0	2.511 ± 0.086	4.2 ± 0.1	0.656 ± 0.013
Aerogel-2	2.522 ± 0.070	3.9 ± 0.1	0.658 ± 0.011
Aerogel-5	2.525 ± 0.070	3.8 ± 0.1	0.658 ± 0.011

Table S5. Pore size of **HRhMOP** and **Aerogel-*n*** estimated by the peaks appearing in WAXS data

Sample	Peak I				Peak II			
	q_{peak}	FWHM	Area	d-space	q_{peak}	FWHM	Area	d-space
HRhMOP	5.17 nm^{-1}	0.19	3.45	1.22 nm	12.71 nm^{-1}	3.29	133.01	0.49 nm
Aerogel-0	4.63 nm^{-1}	0.06	0.09	1.36 nm	12.93 nm^{-1}	2.65	1.02	0.49 nm
Aerogel-1	4.58 nm^{-1}	0.69	0.13	1.37 nm	12.71 nm^{-1}	3.18	1.27	0.49 nm
Aerogel-2	4.65 nm^{-1}	0.70	0.12	1.35 nm	12.68 nm^{-1}	3.48	1.37	0.50 nm
Aerogel-3	4.61 nm^{-1}	0.32	0.04	1.36 nm	12.64 nm^{-1}	3.92	1.67	0.50 nm
Aerogel-4	4.71 nm^{-1}	0.88	0.23	1.33 nm	12.55 nm^{-1}	3.73	1.41	0.50 nm
Aerogel-5	4.84 nm^{-1}	0.63	0.09	1.30 nm	12.58 nm^{-1}	3.47	1.28	0.50nm

5. Computational characterization of the porosity in fully linked MOP crystalline network

1. Computational details

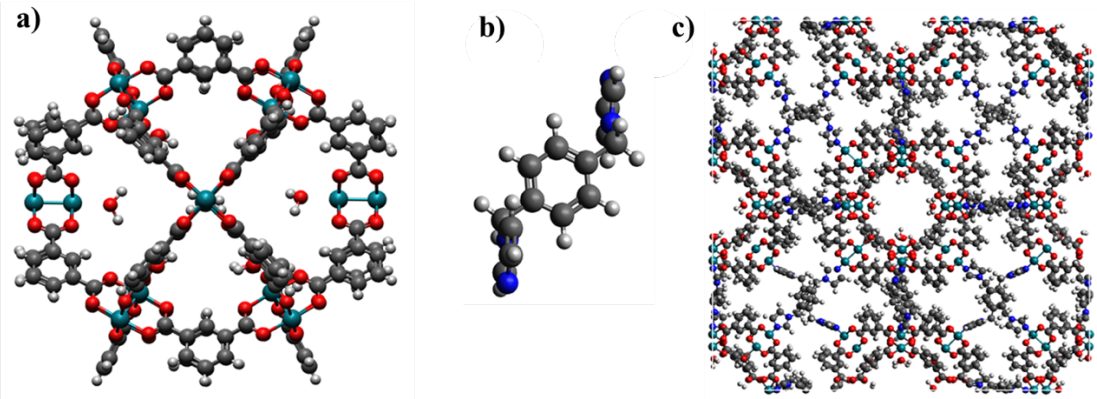

Figure S23. Panel (a) shows the 12-connected MOP with Rh as connection point. Water molecules shown inside of the cage are coordinated to Rh. Panel (b) shows the **bix** linker with nitrogen as connection points. Panel (c) shows the resulting crystalline structure with ***fcu*** topology and the 12-connected **HRhMOP** and **bix** as the linker. C = gray, H = white, O = red, N = blue, and Rh = turquoise. Visualized using Avogadro software[10-11].

Porosity of **HRhMOP** was studied by performing N_2 adsorption simulations at 77K. MOP cages with Rh and bix for the paddlewheel and linker respectively, were mapped onto an ***fcu*** topology using the crystal generator, ToBaCCo 3.0 (https://github.com/tobacco-mofs/tobacco_3.0)[12-15], as shown in Figure S23. The resulting crystallographic information files from ToBaCCo 3.0 were used as input for the LAMMPS Interface[16] code by Boyd and coworkers to generate its corresponding input files with universal force field (UFF)[16] parameters for the LAMMPS[17] software. Structures were then minimized twice using LAMMPS, the first one with the unit cell dimensions constant and the second allowed changes in the unit cell dimensions. The minimized structure from LAAMPS is named as **HRhMOP(bix)$_6$**.

Grand canonical Monte Carlo simulations were performed to calculate nitrogen adsorption isotherms at 77K with the RASPA[18] software. Nitrogen uptake simulations were performed for pressures between 0.01 and 99990 Pa. Each run consisted of 20000 initialization cycles followed by 60000 production cycles. All moves including translation, rotation, reinsertion and swap were attempted with equal probability. For the framework, a single cell was employed and considered as rigid during the adsorption simulation. Nonbonded interactions were modeled using a Lennard-

Jones potential with a cut off of 12.5 Å. UFF was used for all framework atoms and TraPPE[19] was used for the adsorbed molecules. Adsorbate-adsorbate interactions also included Coulombic interactions.

Helium void fraction and available pore volume were calculated using RASPA. Pore size distribution was calculated using the Zeo++[20-25] software while the surface area was calculated using RASPA and Zeo++. Density profiles were calculated using RASPA and visualized using the ParaView[26] software.

Helium void fraction was calculated at 298K using its respective Lennard-Jones parameters[27] and using Widom insertions[28-29]. The result was then used to calculate the available pore volume on the structure. Both helium void fraction and available pore volume calculations were run for 10000 cycles. The surface area obtained from RASPA is calculated by using a nitrogen rolling probe and measuring the amount of overlap between framework atoms. This amount is then multiplied by the area of a sphere and the summation over all atoms in the framework gives the surface area.[18] The run consisted of 10000 cycles at 298K, using a surface area probe distance of σ of the nitrogen probe. Surface area was also obtained from Zeo++, where it is calculated by determining the accessibility of pores followed by a Monte Carlo (MC) sampling procedure to integrate the surface area. To determine accessibility and perform MC sampling a probe with radius of 1.2 Å is used in both cases. A total of 2000 MC samples per atom are used. Pore size distribution is calculated in a similar fashion as the surface area, but the MC samples are per unit cell instead of atoms in the framework. A total of 10000 MC samples per unit cell are used. Likewise, probes of radius of 1.2 Å are used for both cases.

Density profiles were calculated for **HRhMOP(bix)$_6$** at 77K and selected pressures: 2.5, 2510, and 15850 Pa. The number of cycles and initialization cycles were 10000 and the restart file from the adsorption simulation was used.

2. Results and discussion

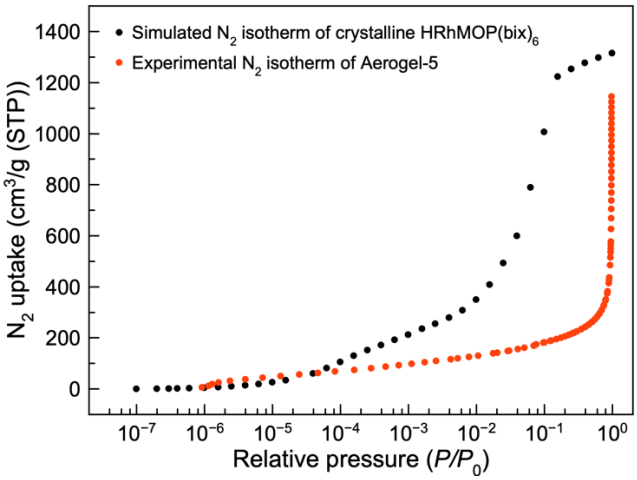

Figure S24. N_2 adsorption isotherm at 77K for the minimized **HRhMOP(bix)$_6$** structure

We studied the adsorption of nitrogen in the **HRhMOP(bix)$_6$** structures with the ***fcu*** topology and compared experimental and computational results. First, the helium void fraction and pore volume were calculated as 0.85 and 2.05 $cm^3\ g^{-1}$, respectively. The values for the pore volume are higher than the ones obtained experimentally with the Aerogels, in which the highest value was 1.77 for **Aerogel-5**, as shown in Table S6. The surface area obtained computationally is significantly different than the ones obtained experimentally for the different aerogel samples. The highest value experimentally obtained was 758.11 $m^2\ g^{-1}$ for **Aerogel-5** and it is around five times smaller than the values obtained from RASPA and Zeo++. Differences on the results between software packages are due to the way that the surface area is calculated. **HRhMOP(bix)$_6$** adsorbs 1315.9 $cm^3\ g^{-1}$, as shown in Figure S24, while **Aerogel-0** adsorbs 1075.5 $cm^3\ g^{-1}$.

Table S6. Comparison of experimental and computational surface area and total pore volume.

Structure	Surface Area ($m^2\ g^{-1}$)	Pore Volume ($cm^3\ g^{-1}$)	Adsorption at P/P_0 ~1 ($cm^3\ g^{-1}$)
HRhMOP	665.32	0.3841	248.3
Aerogel-0	564.78	1.6636	1075.5
Aerogel-2	676.51	1.4179	916.7
Arogel-5	758.11	1.7726	1146.0
HRhMOP(bix)$_6$ R*	3706.38	2.0542	1315.9
HRhMOP(bix)$_6$ Z*	3985.18	1.59	-

Pore size distribution (PSD) estimated by Zeo++ for **HRhMOP(bix)$_6$** is shown in Figure S25. The PSD for **HRhMOP(bix)$_6$** gives a small peak around 0.95 nm corresponding to MOP cavities. Five peaks around 1.64 and 1.89 nm correspond to a distribution of pore sizes between the interlinked MOPs. Similarly, it gives two broad peaks at 2.45 and 2.52 nm corresponding to largest pore on the center of the network.

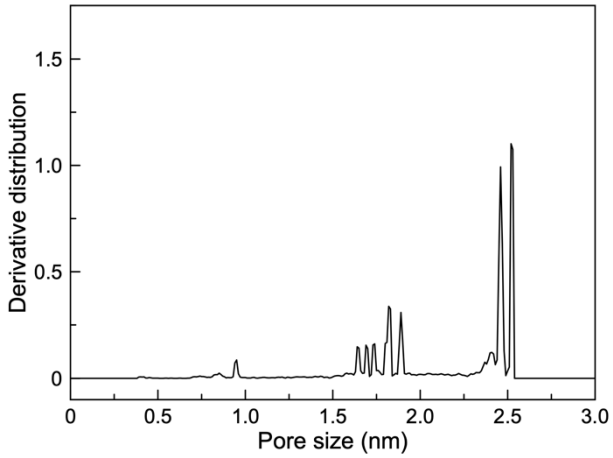

Figure S25. Pore size distribution for the **HRhMOP(bix)$_6$** structure calculated by using the Zeo++[20-25] software.

Density profiles (Figure S26) show how the N_2 first starts to occupy the MOP pores at a pressure of 2.5 Pa. At a pressure of 2510 Pa, N_2 occupies the pores between the interlinked MOPs. Lastly, at a pressure of 15850 Pa all the pores are occupied by N_2.

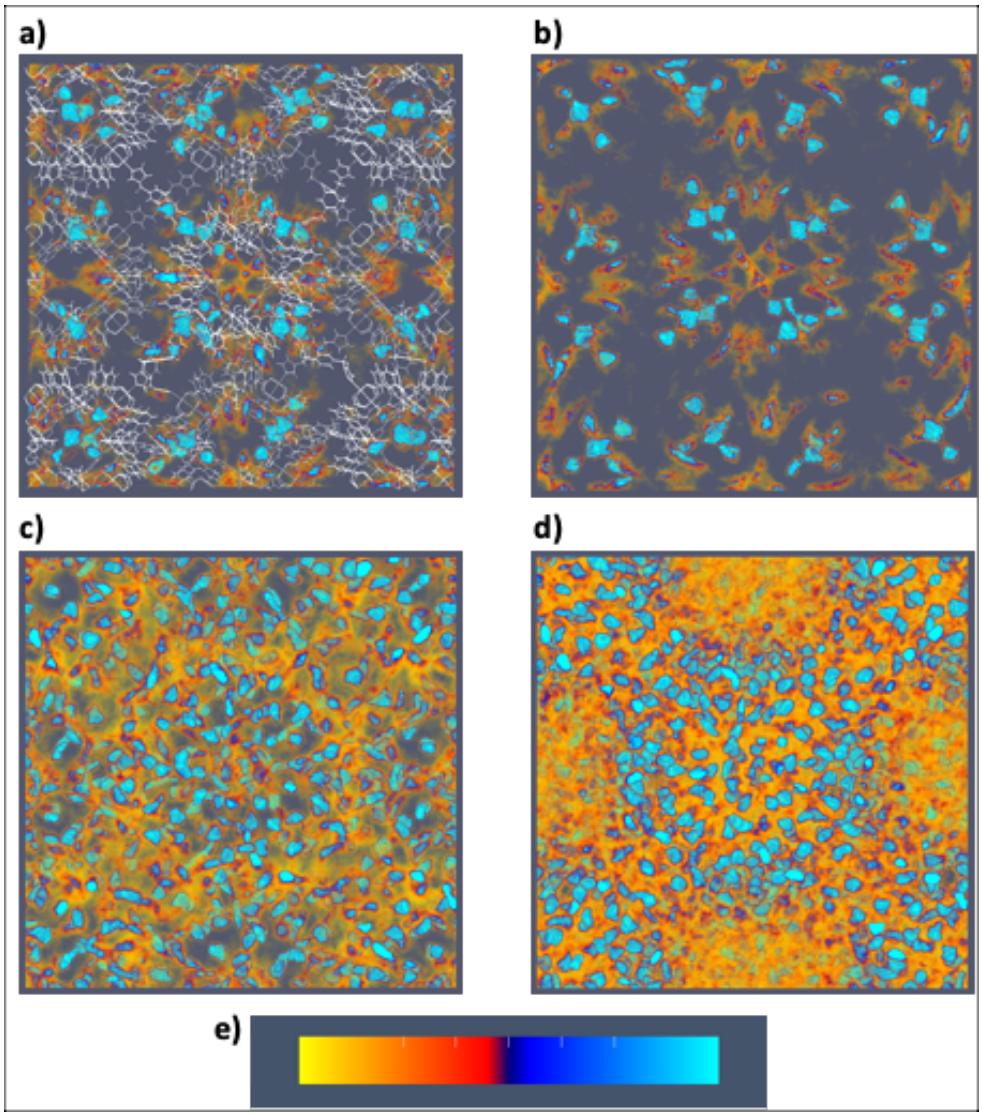

Figure S26. (a) Density profile for **HRhMOP(bix)$_6$** with atomic structure at 2.5 Pa of N_2. (b) Low density profile for **HRhMOP(bix)$_6$** at 2.5 Pa of N_2. (c) Medium density profile for **HRhMOP(bix)$_6$** at 2510 Pa of N_2. (d) High density profile for **HRhMOP(bix)$_6$** at 15850 Pa of N_2. (e) The legend of the color profile from the lowest (yellow) to the highest (cyan) N_2 concentration.

REFERENCES

1. Furukawa, S.; Horike, N.; Kondo, M.; Hijikata, Y.; Carné-Sánchez, A.; Larpent, P.; Louvain, N.; Diring, S.; Sato, H.; Matsuda, R., Rhodium–Organic Cuboctahedra as Porous Solids with Strong Binding Sites. *Inorg. Chem.* **2016,** *55* (21), 10843-10846.
2. Kansy, J., Microcomputer Program for Analysis of Positron Annihilation Lifetime Spectra. *Nucl. Instrum. Methods Phys. Res. A.* **1996,** *374* (2), 235-244.
3. Smales, G. J.; Pauw, B. R., The MOUSE Project: A Meticulous Spproach for Obtaining Traceable, Wide-Range X-ray Scattering Information. *J. Instrum.* **2021,** *16* (06), P06034.
4. Pauw, B. R.; Smith, A. J.; Snow, T.; Terrill, N. J.; Thunemann, A. F., The Modular Small-Angle X-Ray Scattering Data Correction Sequence. *J. Appl. Crystallogr.* **2017,** *50* (6), 1800-1811.
5. Filik, J.; Ashton, A. W.; Chang, P. C. Y.; Chater, P. A.; Day, S. J.; Drakopoulos, M.; Gerring, M. W.; Hart, M. L.; Magdysyuk, O. V.; Michalik, S.; Smith, A.; Tang, C. C.; Terrill, N. J.; Wharmby, M. T.; Wilhelm, H., Processing Two-Dimensional X-Ray Diffraction and Small-Angle Scattering Data in DAWN 2. *J. Appl. Crystallogr.* **2017,** *50* (3), 959-966.
6. Bressler, I.; Pauw, B. R.; Thunemann, A. F., McSAS: Software for the Retrieval of Model Parameter Distributions from Scattering Patterns. *J. Appl. Crystallogr.* **2015,** *48* (3), 962-969.
7. Carné-Sánchez, A.; Craig, G. A.; Larpent, P.; Hirose, T.; Higuchi, M.; Kitagawa, S.; Matsuda, K.; Urayama, K.; Furukawa, S., Self-Assembly of Metal–Organic Polyhedra into Supramolecular Polymers with Intrinsic Microporosity. *Nat. Commun.* **2018,** *9* (1), 1-8.
8. Carné-Sánchez, A.; Craig, G. A.; Larpent, P.; Guillerm, V.; Urayama, K.; Maspoch, D.; Furukawa, S., A Coordinative Solubilizer Method to Fabricate Soft Porous Materials from Insoluble Metal–Organic Polyhedra. *Angew. Chem. Int. Ed.* **2019,** *131* (19), 6413-6416.
9. Zhukhovitskiy, A. V.; Zhong, M.; Keeler, E. G.; Michaelis, V. K.; Sun, J. E. P.; Hore, M. J. A.; Pochan, D. J.; Griffin, R. G.; Willard, A. P.; Johnson, J. A., Highly Branched and Loop-Rich Gels via Formation of Metal–Organic Cages Linked by Polymers. *Nat. Chem.* **2016,** *8* (1), 33-41.
10. Avogadro: An Open-Source Molecular Builder and Visualization Tool. Version 1.XX. http://avogadro.cc/.
11. Hanwell, M. D.; Curtis, D. E.; Lonie, D. C.; Vandermeersch, T.; Zurek, E.; Hutchison, G. R., Avogadro: An Advanced Semantic Chemical Editor, Visualization, and Analysis Platform. *J. Cheminformatics* **2012,** *4* (1), 17.
12. Gómez-Gualdrón, D. A.; Colón, Y. J.; Zhang, X.; Wang, T. C.; Chen, Y.-S.; Hupp, J. T.; Yildirim, T.; Farha, O. K.; Zhang, J.; Snurr, R. Q., Evaluating Topologically Diverse Metal–Organic Frameworks for Cryo-Adsorbed Hydrogen Storage. *Energy Environ. Sci.* **2016,** *9* (10), 3279-3289.
13. Colón, Y. J.; Gómez-Gualdrón, D. A.; Snurr, R. Q., Topologically Guided, Automated Construction of Metal–Organic Frameworks and Their Evaluation for Energy-Related Applications. *Cryst. Growth Des.* **2017,** *17* (11), 5801-5810.
14. O'Keeffe, M.; Peskov, M. A.; Ramsden, S. J.; Yaghi, O. M., The Reticular Chemistry Structure Resource (RCSR) Database of, and Symbols for, Crystal Nets. *Acc. Chem. Res.* **2008,** *41* (12), 1782-1789.
15. Anderson, R.; Gómez-Gualdrón, D. A., Increasing Topological Diversity During Computational "Synthesis" of Porous Crystals: How and Why. *CrystEngComm* **2019,** *21* (10), 1653-1665.
16. Boyd, P. G.; Moosavi, S. M.; Witman, M.; Smit, B., Force-Field Prediction of Materials Properties in Metal-Organic Frameworks. *J. Phys. Chem. Lett.* **2017,** *8* (2), 357-363.
17. Plimpton, S., Fast Parallel Algorithms for Short-Range Molecular Dynamics. *J. Comput. Phys* **1995,**

117 (1), 1-19.
18. Dubbeldam, D.; Calero, S.; Ellis, D. E.; Snurr, R. Q., RASPA: Molecular Simulation Software for Adsorption and Diffusion in Flexible Nanoporous Materials. *Mol. Simul.* **2016,** *42* (2), 81-101.
19. Martin, M. G.; Siepmann, J. I., Transferable Potentials for Phase Equilibria. 1. United-Atom Description of n-Alkanes. *J. Phys. Chem. B* **1998,** *102* (14), 2569-2577.
20. Martin, R. L.; Smit, B.; Haranczyk, M., Addressing Challenges of Identifying Geometrically Diverse Sets of Crystalline Porous Materials. *J. Chem. Inf. Model.* **2012,** *52* (2), 308-318.
21. Willems, T. F.; Rycroft, C. H.; Kazi, M.; Meza, J. C.; Haranczyk, M., Algorithms and Tools for High-Throughput Geometry-Based Analysis of Vrystalline Porous Materials. *Micropor. Mesopor. Mater.* **2012,** *149* (1), 134-141.
22. Pinheiro, M.; Martin, R. L.; Rycroft, C. H.; Jones, A.; Iglesia, E.; Haranczyk, M., Characterization and Comparison of Pore Landscapes in Crystalline Porous Materials. *J. Mol. Graph. Model.* **2013,** *44*, 208-219.
23. Pinheiro, M.; Martin, R. L.; Rycroft, C. H.; Haranczyk, M., High Accuracy Geometric Analysis of Crystalline Porous Materials. *CrystEngComm* **2013,** *15* (37), 7531-7538.
24. Martin, R. L.; Haranczyk, M., Construction and Characterization of Structure Models of Crystalline Porous Polymers. *Cryst. Growth Des.* **2014,** *14* (5), 2431-2440.
25. Ongari, D.; Boyd, P. G.; Barthel, S.; Witman, M.; Haranczyk, M.; Smit, B., Accurate Characterization of the Pore Volume in Microporous Crystalline Materials. *Langmuir* **2017,** *33* (51), 14529-14538.
26. Ahrens, J.; Geveci, B.; Law, C. In *ParaView: An End-User Tool for Large-Data Visualization*, The Visualization Handbook, 2005.
27. Talu, O.; Myers, A. L., Molecular Simulation of Adsorption: Gibbs Dividing Surface and Comparison with Experiment. *AIChE Journal* **2001,** *47* (5), 1160-1168.
28. Widom, B., Some Topics in the Theory of Fluids. *The J. Chem. Phys.* **1963,** *39* (11), 2808-2812.
29. Dullens *, R. P. A.; Aarts, D. G. A. L.; Kegel, W. K.; Lekkerkerker, H. N. W., The Widom Insertion Method and Ordering in Small Hard-Sphere Systems. *Mol. Phys.* **2005,** *103* (21-23), 3195-3200.